Triangular cross-section grating couplers for integrated quantum nanophotonic hardware in silicon carbide

Pranta Saha,[1] Sridhar Majety,[1] Scott Dhuey,[2] and Marina Radulaski[1]
[1)]*Electrical and Computer Engineering Department, University of California, Davis, CA 95616, USA*
[2)]*The Molecular Foundry, Lawrence Berkeley National Laboratory, 1 Cyclotron Rd, Berkeley, CA 94720, USA*

(*Electronic mail: prsaha@ucdavis.edu)

Triangular cross-section nanodevices are among the leading approaches for integrating color centers with photonics for applications in quantum information processing. We design periodic and aperiodic fishbone triangular grating couplers in silicon carbide. We optimize the designs for achieving up to $\sim 31\%$ collection efficiency from color center integrated triangular devices to a microscopy system. Using an ion beam angle etching process, we demonstrate proof-of-principle fabrication of the designed devices for future implementation in wafer-scale quantum nanophotonics.

I. INTRODUCTION

Quantum networks require a medium that can store quantum information for a long time and provide an interface to transfer the information reliably over long distances. Photons are excellent quantum information carriers as they experience low loss and less decoherence when transmitted through optical fiber networks, making it easier to integrate quantum networks into existing infrastructure[1–3]. Color centers, luminous defects in wide band gap semiconductors[4], have sparked interest within the quantum community due to their spin-photon interface where the electron or nuclear spin acts as a stationary qubit and spin-entangled photon acts as a flying qubit[5]. For quantum networks and distributed quantum information processing (QIP), color centers in silicon carbide (SiC) are particularly interesting as they generate spin-entangled photons near telecom band wavelengths[6] with seconds long spin coherence times[7] and ultra-narrow inhomogeneous broadening[8]. Moreover, compatibility with silicon-based device fabrication processes and availability of high-purity wafer-scale substrates make SiC a potential platform for scalable QIP hardware.

Color centers are required to be integrated with nanophotonic devices to perform on-chip QIP[6,9]. In this regard, suspended photonics paves the way for higher optical confinement due to maximum refractive index contrast with the surrounding medium. Previous efforts in fabricating color center integrated SiC suspended devices either limited the performance of color center optical coherence[10] or encountered scaling issues[6]. As color centers exhibit excellent spectral stability in bulk substrates[11], the angle-etching method has emerged as a promising technique to fabricate bulk freestanding nanostructures for color center integration. Angle-etching can be implemented either by a Faraday cage or by ion beam etching (IBE). In this method, ions are directed at an angle toward the substrate to undercut the nanophotonic structures which results in a triangular cross-section profile. SiC color center photonics and spintronics in this non-conventional triangular geometry have demonstrated robust performance for QIP applications[12–16].

Recently, we have developed a reactive ion beam etching (RIBE) process for wafer-scale integration of triangular cross-section photonic devices with color centers in SiC[17]. An on-chip wafer-scale testing mechanism is required for characterizing color center interaction with triangular shaped nanophotonic hardware. Although edge couplers offer highly efficient coupling over a large bandwidth, they do not support wafer-level testing and have complex post-fabrication steps with limited access to the circuits[18,19]. Vertical grating coupler (GC) is a convenient choice for flexible integration with other photonic elements on the same chip, consequently, allowing for wafer-scale testing. Fiber-based GCs exhibit excellent coupling efficiency at the cost of large footprints and precise fiber alignment[19]. As cryogenic environment is required for color center characterization[20], free-space GCs in combination with microscope objective have proven to be a very practical solution[21,22]. Typical microscopy systems have a higher numerical aperture (NA) compared to optical fibers and provide wider bandwidth[23]. Moreover, due to the absence of mode mismatch issues between the fiber core and the GC, free-space GCs can be optimized for a compact layout.

In this work, we conduct a thorough study on free-space SiC triangular cross-section suspended GC in light of color center quantum nanophotonics. Fig. 1(a) shows a perspective illustration of color center coupling characterization with integrated GC. First, we describe the important parameters of the GC and evaluate their performance using Finite-Difference Time-Domain (FDTD) simulations. As we intend to utilize the wafer-scale RIBE process for device fabrication, we incorporate the fabrication constraints in our design. Next, we optimize the design to maximize the collection efficiency from color center emission through a microscope objective and discuss coupling dynamics in the triangular geometry. In the end, we demonstrate the fabrication of the triangular cross-section GC using the RIBE process.

II. TRIANGULAR CROSS-SECTION FISHBONE GRATING COUPLER

In this section, we analyze the design parameters for triangular cross-section suspended GC in SiC. Our triangular cross-section GC consists of (i) a triangular waveguide, (ii) an adiabatically tapered region, and (iii) a fishbone like grating structure. We choose the fishbone grating design in accor-

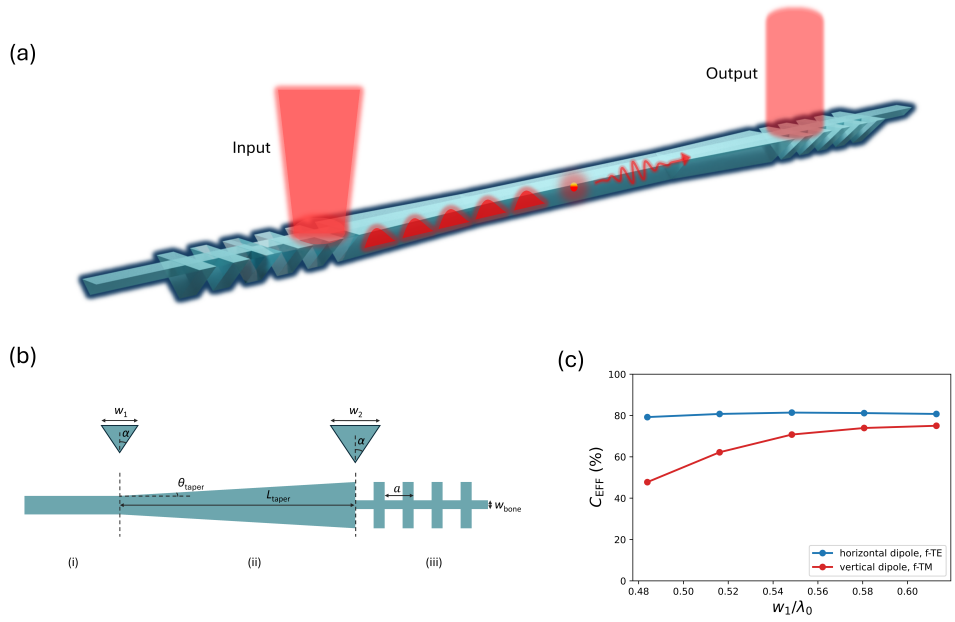

FIG. 1. (a) A perspective figure of the triangular cross-section grating couplers (GCs) used for the characterization of color center coupling with integrated nanophotonic hardware. The red sphere at the center of the waveguide represents the color center. (b) Top view of triangular cross-section fishbone GC with three regions: (i) waveguide, (ii) adiabatic taper, and (iii) fishbone grating. (c) Coupling efficiency (C_{EFF}) of horizontal and vertical dipoles into the fundamental transverse electric (f-TE) and the fundamental transverse magnetic (f-TM) modes, respectively, of triangular waveguides with etch angle, $\alpha = 45^{\circ}$.

dance with the fabrication compatibility of the RIBE process to produce wafer-scale triangular cross-section devices. Fig. 1(b) shows the top view schematic of the GC with waveguide width w_1, etch angle (half angle at the apex) α, taper angle θ_{taper}, taper length L_{taper}, maximum taper width w_2, grating period a, and the central bone width w_{bone}. The refractive index of SiC is kept $n_{\mathrm{SiC}} = 2.6$ throughout the analysis. We parameterize the scales w.r.t. wavelength of interest λ_0 to make the design scalable for the variety of color centers SiC hosts. We optimize each component individually to achieve the most efficient design.

A. Single-mode waveguide

Single-mode propagation is an important requirement in the waveguide design for performing on-chip QIP[24,25]. For each α, there exists an optimal width for single-mode propagation in the triangular cross-section waveguides[13]. In this work, we choose $\alpha = 45^{\circ}$ as it offers higher confinement[15] and coupling[13,16] compared to other etch angles that have been fabricated with the RIBE process in SiC[17]. Based on the dipole orientation in the SiC crystal lattice, color center emission can couple to fundamental transverse electric (f-TE), fundamental transverse magnetic (f-TM), and other higher-order modes supported by the triangular waveguide. Hence, we optimize the triangular waveguide width w_1 for maintaining single-mode propagation of both horizontal and vertical electric dipole radiations with high coupling efficiency (C_{EFF}) using Lumerical FDTD package as shown in Fig. 1(c). We position the dipole sources with emission wavelength λ_0 at the centroid of the triangle which is the optimum color center position in triangular geometry for the best coupling to the waveguide modes[12–14]. We pre-select the w_1 range using Lumerical MODE (Finite-Difference Eigensolver) package so that the horizontal (vertical) dipole couples only to the f-TE (f-TM) mode. Although the proposed design is a 1D-GC structure in which we can optimize only for a single state of polarization[19], we choose $w_1 = 0.548\lambda_0$ to obtain high C_{EFF} for both dipole orientations.

B. Adiabatic taper

An adiabatically tapered region is instrumental to coupling light in and out of the chip[26]. It allows for a smooth transition of light from the waveguide mode to the Gaussian mode by gradually changing the size and shape of the optical mode along the taper. The slow transition of the effective refractive index (n_{eff}) of the waveguide cross-section ensures minimal mode conversion to higher-order or radiation modes resulting in high coupling efficiency. Traditional fiber-coupled GCs require very long taper regions to match the mode field diameter of the single-mode optical fibers[18]. On the other hand, light coupling through the microscope objective enables very compact designs for such tapers as the focused Gaussian beam

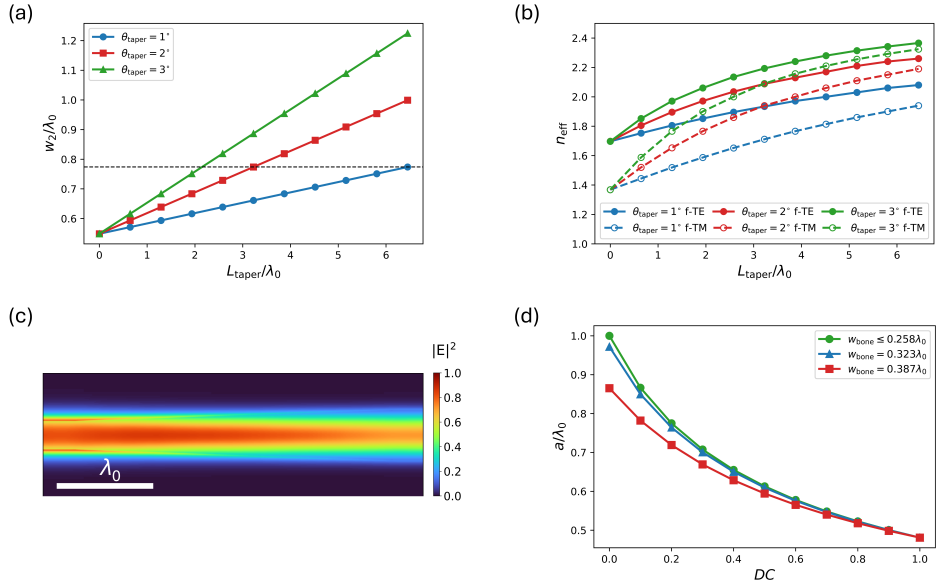

FIG. 2. (a) Taper width w_2 w.r.t taper length L_{taper} for taper angles $\theta_{\text{taper}} = 1°, 2°, 3°$. The dashed (black) line shows the fabrication constraint imposed on w_2. (b) Effective refractive indices n_{eff} of the f-TE and the f-TM modes along L_{taper} for $\theta_{\text{taper}} = 1°, 2°, 3°$. (c) Top view cross-section of the electric field (E-field) intensity ($|\text{E}|^2$) profile for the adiabatic taper design with $\theta_{\text{taper}} = 2°$, $L_{\text{taper}} = 3.225\lambda_0$, and $w_2 = 0.774\lambda_0$ where the f-TE mode of the waveguide with $w_1 = 0.548\lambda_0$ is injected into the taper region. The cross-section is taken at the centroid plane of the maximum taper width w_2. (d) Grating period a and duty cycle DC which satisfy the 1st order vertical grating phase matching condition for $w_{\text{bone}} = 0.258\lambda_0, 0.323\lambda_0, 0.387\lambda_0$.

spot size becomes orders of magnitude smaller compared to the optical fiber mode.

In the SOI platform, it has been observed that linear tapers with very small taper angle (θ_{taper}) result in higher transmission[27]. We apply a similar strategy in designing the triangular cross-section taper region by linearly increasing the taper width for $\theta_{\text{taper}} = 1°, 2°, 3°$, shown in Fig. 2(a). To ensure gradual change in n_{eff} of the waveguide mode, we calculate the n_{eff} of the f-TE and f-TM modes (mode #1 and mode #2, respectively) of the triangular waveguide along L_{taper}. Fig. 2(b) demonstrates that the adiabatic condition for triangular waveguides[28]: $dn/dx < (2\pi/\lambda_0)|n_{\text{eff},1}(x) - n_{\text{eff},2}(x)|^2$, where n is the effective index of the waveguide cross-section with maximum taper width w_2 and $n_{\text{eff},i}$ is the effective index of the ith waveguide mode along L_{taper}, is satisfied for all three θ_{taper}. However, owing to the etch selectivity of the mask in the developed RIBE wafer-scale process[17], we restrict w_2 to be $0.774\lambda_0$, $\sim 40\%$ larger than w_1, for undercutting both w_1 and w_2 cross-section profiles in a single etch. Although all three θ_{taper} designs exhibit unity transmission for the f-TE mode injection from the waveguide, we choose $\theta_{\text{taper}} = 2°$ leading to $L_{\text{taper}} = 3.225\lambda_0$ for $w_2 = 0.774\lambda_0$.

C. Fishbone grating

Refractive index variation with periodic configuration in the direction of light propagation is the most preferred approach for breaking the device symmetry to achieve out-of-plane coupling through diffraction[18]. Our fishbone grating is constructed by varying the width of the triangular cross-section periodically to implement refractive index contrast. The central bone ensures the mechanical stability of the suspended structure. The diffraction mechanism for a GC is governed by Bragg phase matching condition: $N_{\text{eff}} - n_{\text{air}}\sin\theta = m\lambda_0/a$, where N_{eff} is the effective index of the guided mode in the grating medium, n_{air} is the refractive index of air, θ is the diffraction angle, m is the grating order, λ_0 is the target wavelength, and a is the grating period. For 1D-GC, the 1st order diffracted mode is vertically emitted from the grating[19]. Hence, with $\theta = 0°$ and $m = 1$, we can achieve vertical outcoupling and the phase matching condition reduces to $a = \lambda_0/N_{\text{eff}}$. Due to the 1D periodicity, we can optimize for only one polarization state, in our case the f-TE mode. We estimate the N_{eff} using the analytical expression[29]: $N_{\text{eff}} = \sqrt{(1-DC)n_1^2 + DCn_2^2}$, where DC is the duty cycle, or the fill factor, of the wider section, and n_1 and n_2 are the effective indices of the triangular cross-section with widths w_{bone} and w_2, respectively. The grating period a and duty cycle DC that satisfy the phase matching condition for different w_{bone} values are presented in Fig. 2(d). We observe

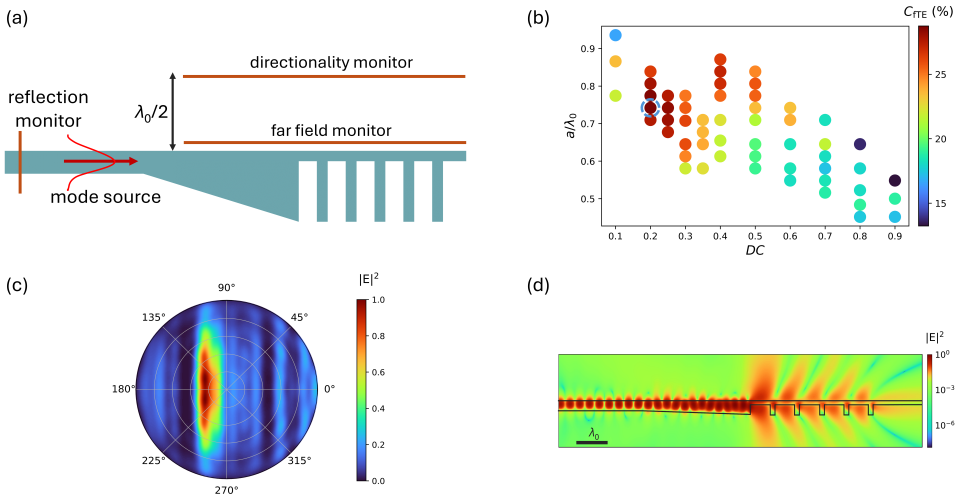

FIG. 3. (a) Side view of the FDTD simulation setup for calculating collection efficiency. (b) Collection efficiency (C_{fTE}) for the f-TE mode injection from waveguide with variation in DC and a. The dashed (blue) circle indicates the most optimized design for the maximum C_{fTE}. (c)-(d) The far field radiation pattern and the side view cross-section $|\mathrm{E}|^2$ distribution, respectively, of the triangular GC with $DC = 0.2$ and $a = 0.742\lambda_0$, marked with blue dashed circle in (b).

that there exists no physical mode in the triangular cross-section for $w_{\mathrm{bone}} \leq 0.258\lambda_0$ at λ_0 which means the effective index of the narrow regions is $n_1 = 1$. Therefore, we choose $w_{\mathrm{bone}} = 0.258\lambda_0$ for obtaining maximum index contrast.

III. DESIGN OPTIMIZATION

The GC design optimization is focused on enhancing the collection efficiency from color center integrated nanophotonic devices for characterizing light-matter interaction. Fig. 3(a) shows the side view of the 3D FDTD simulation setup for calculating the collection efficiency. We use a mode source to inject the f-TE mode of the waveguide (width w_1) at λ_0 into the grating. A field and power monitor is placed above the triangular cross-section GC at a $\lambda_0/2$ distance for measuring the fraction of power going in the upward direction. As we are interested in maximizing the light collection through a microscope objective, we add another field and power monitor very close to the top surface of the GC to calculate the far field radiation pattern and subsequently the fraction of power collected by an objective with a given NA (0.65 in this work). The collection efficiency is obtained by multiplying the power fractions calculated from these two monitors. We use a field and power monitor before the source to check the amount of light reflected back into the waveguide.

For a given design, the collection increases with the number of gratings and saturates for 5 unit cells. As a result, we use 5 grating periods for all the GCs in our analysis. Fig. 3(b) exhibits the collection efficiencies (C_{fTE}) from the injected f-TE waveguide mode with variation in DC and a. We observe that reflection decreases with the increase in C_{fTE}. The maximum C_{fTE} is $\sim 29\%$, acquired from a design with $DC = 0.2$ and $a = 0.742\lambda_0$. The obtained C_{fTE} value is comparable to another compact GC design realized in silicon nitride platform for microscope objective collection where the theoretical coupling efficiency reaches up to 40% (60% with a reflective mirror coating on the substrate)[23]. Notably, the most efficient design does not satisfy the phase matching condition which can stem from the broken symmetry of the triangular profile compared to rectangular structures. This phenomenon is observed in another theoretical work with triangular cross-section GCs in gallium nitride[30]. Fig. 3(c)-(d) shows the far field radiation pattern and side view cross-section of electric field intensity ($|\mathrm{E}|^2$) distribution, respectively, at λ_0 for the most efficient design. We also simulate the collection efficiency of the optimized design as a function of normalized wavelength λ/λ_0. The collection efficiency for the f-TM mode at λ_0 is $\sim 13\%$, lower than half of C_{fTE}, which is expected. Conventional 1D grating couplers have to deal with bandwidth issues[31,32] whereas the triangular cross-section GC broadband response appears flat, meaning the same design can be utilized for studying different zero-phonon line (ZPL) emissions from a color center in SiC. To characterize the incoupling efficiency of the optimized design, we employ a Gaussian source focused from above by an objective with 0.65 NA and a power monitor in the waveguide region as shown in Fig. 4(b). For higher incoupling, the source needs to be focused on the first grating period. Focusing on other unit cells results in lower incoupling as a large amount of light readily couples to the guided mode of the adiabatic taper as seen in Fig. 4(d). The s-polarized Gaussian beam mostly couples to the f-TE mode while the p-polarized beam couples mostly to

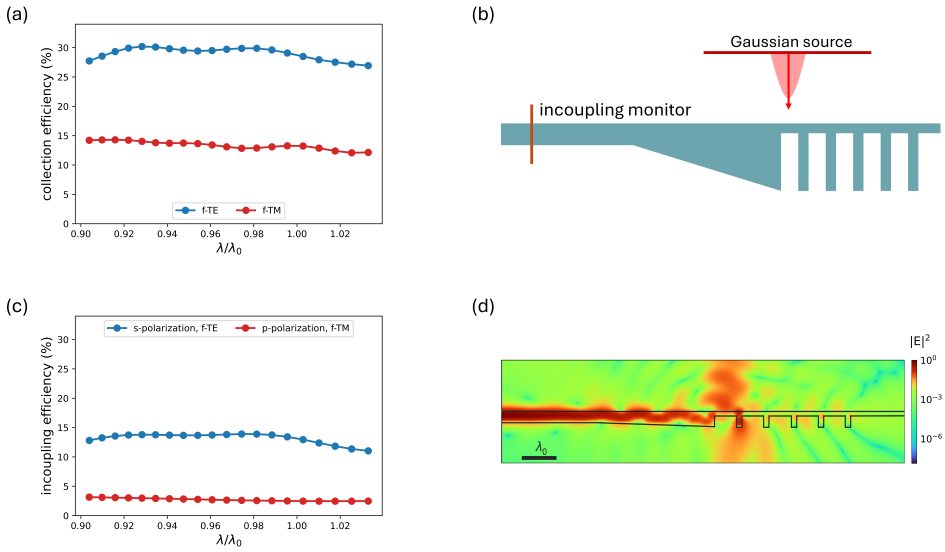

FIG. 4. (a) Collection efficiency of the optimized design with periodic grating for the f-TE and f-TM modes as a function of normalized wavelength λ/λ_0. (b) Side view of the FDTD simulation setup for calculating the incoupling efficiency. (c) Incoupling efficiency for the s-polarized and p-polarized Gaussian beams as a function of normalized wavelength λ/λ_0. (d) The side view cross-section $|E|^2$ distribution of the triangular GC for an s-polarized Gaussian beam focused from above at λ_0.

the f-TM mode. Although we observe some initial coupling to high-order modes, they diminish as the incoupled light propagates through the waveguide. Fig. 4(c) illustrates the broadband response for the incoupling efficiency of the optimized design. The incoupling efficiency is much lower than outcoupling as our optimization technique prioritizes the collection efficiency.

Non-uniform GCs have proven to be very effective in enhancing the overall efficiency[19,33,34]. Non-uniformity is generally introduced by linearly apodizing the *DC* or a along the direction of propagation. In search of the most optimized design, we opt for a similar technique. Keeping $a = 0.742\lambda_0$ constant, we linearly change the *DC* of each unit cell with the following equation: $DC_i = DC_0 \pm r \times i$, where r is the apodization factor, $DC_0 = 0.2$, and $i = 0,1,2,3,4$. However, we observe the C_{fTE} slowly decreasing for both cases with variation in r from 0 to 0.02. On the other hand, we linearly change a for each grating section, with constant $DC = 0.2$, by the following equation: $a_i = a_0(1 \pm f \times i)$, where f is the aperiodic factor, $a_0 = 0.742\lambda_0$, and $i = 0,1,2,3,4$. Fig. 5(a) demonstrates that C_{fTE} gradually increases (decreases) with increasing (decreasing) a and starts to decrease (increase) after reaching an inversion point. We notice that even for the most optimized aperiodic design, with $f = 0.07$, C_{fTE} only increases by $\sim 2\%$. However, we observe a significant change in the broadband response, Fig. 5(b), and the far field radiation pattern, Fig. 5(d), of the aperiodic GC. The far field radiation appears less dispersive compared to the periodic design. While collection and incoupling efficiencies for the f-TM mode remain invariant for the aperiodic optimization, the broadband response for the f-TE mode becomes a normal distribution. Based on the specific application requirement, one can adopt either the periodic or the aperiodic design as both designs exhibit comparable collection efficiencies.

IV. PROOF-OF-PRINCIPLE FABRICATION AND DISCUSSION

Designed grating couplers can readily be implemented with the wafer-scale quantum nanophotonic fabrication processes. As illustrated in Fig. 1(a), we envision fabricating a suspended triangular waveguide with grating couplers positioned on both ends. One coupler is used to direct the laser into the waveguide and stimulate the color center with off-resonant excitation. The other one couple both the excitation light and the color center emission out into a microscopy system where the excitation beam is selectively filtered out. With this mechanism, light-matter interaction in the triangular geometry can be experimentally characterized for all the suspended active and passive photonic devices.

We test the key step in the fabrication of the studied GC designs in SiC with the RIBE process. In this method, a collimated and uniform beam of high energy reactive and inert gas ions are directed toward a substrate holder that can be rotated and tilted at an angle. The tilt of the substrate holder defines the α of the triangular cross-section and the rotation ensures a uniform device undercut. The presence of physical etch, due to the inert gas ions, reduces the mask etch selectivity as well as causes higher re-deposition from the sputtered material which makes the etching process slower. Hence, we have considered these constraints in our designs as explained in Section II.

We choose $\lambda_0 = 1243$ nm, one of the ZPL emissions from

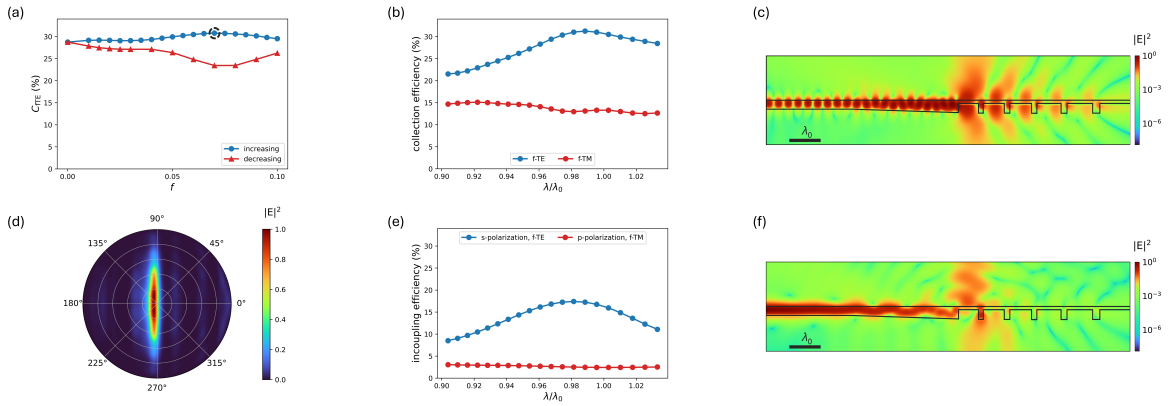

FIG. 5. (a) C_{fTE} with variation in aperiodic factor f for linear increase and decrease of a. The dashed (black) circle shows the most efficient aperiodic design for the maximum CfTE. (b) Collection efficiency of the optimized design with aperiodic grating, marked with a black circle in (a), as a function of normalized wavelength λ/λ_0. (c)-(d) The side view cross-section $|\mathrm{E}|^2$ distribution and the far field radiation pattern, respectively, of the triangular aperiodic GC with $f = 0.07$ at λ_0. (e) Incoupling efficiency for the s-polarized and p-polarized Gaussian beams as a function of normalized wavelength λ/λ_0 for the optimized aperiodic GC. (f) The side view cross-section $|\mathrm{E}|^2$ distribution of the triangularly shaped aperiodic GC for an s-polarized Gaussian beam focused from above at λ_0.

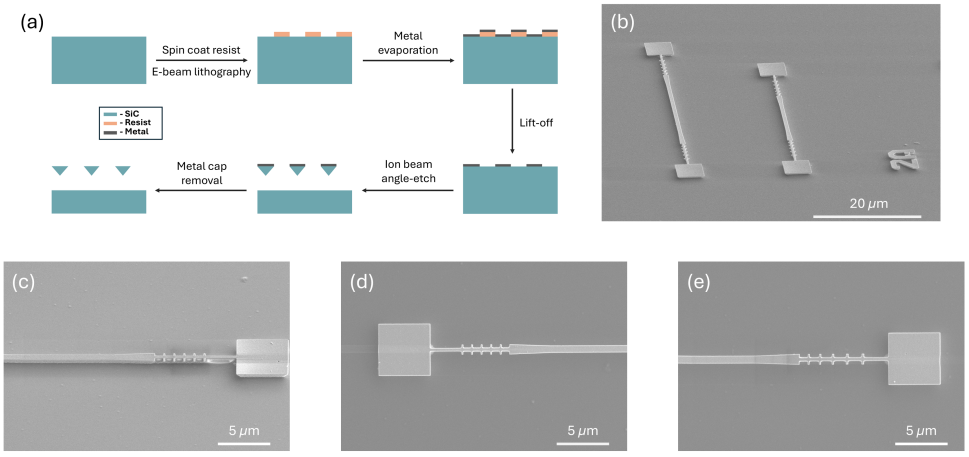

FIG. 6. (a) Fabrication process flow of triangular cross-section fishbone GC in SiC. (b)-(c) SEM images of triangular cross-section aperiodic and periodic GCs, respectively, with a 52° tilted view. (d)-(e) Top view SEM images of periodic and aperiodic GCs, respectively. All the SEM images are obtained with the nickel hard mask on top of the devices.

NV center in 4H-SiC, for both the periodic and aperiodic GC fabrication. Fig. 6(a) shows the nanofabrication process flow. We use electron beam lithography for defining the GC patterns on 4H-SiC substrate. Then, we deposit 120 nm thick nickel as a hard metal mask using electron beam evaporation and transfer the GC patterns on to the mask through a lift-off process. The triangular cross-section waveguides and GCs are then fabricated by the RIBE process using SF_6, O_2, and Ar gas ions. During the etching process, we deliberately set the substrate tilt angle to 60° for obtaining $\alpha = 45°$[17]. The SEM images of the fabricated GCs are presented in Fig. 6(b)-(e). We observe that the undercut in these devices are ~ 250 nm, after an hour of etching, which can be a bottleneck for experimental characterization as a significant amount of light can couple to the bulk. This issue can be resolved by performing a prolonged etch. However, a practical robust solution can be the inclusion of inductively coupled plasma-reactive ion etching (ICP-RIE) in the fabrication process flow. The etch rate for ICP-RIE, with the same SF_6 and O_2 chemistry, is much higher compared to the RIBE process. As a result, performing a ver-

tical etch with ICP-RIE, before the angle-etching step, can result in a deeper undercut essential for experimental characterization of the fabricated devices.

Triangular cross-section photonic devices can be fabricated at a wafer-scale in SiC with the RIBE process. This process preserves color center optical properties which facilitates the implementation of on-chip QIP with integrated quantum photonic mesh architecture. With the addition of the proposed GCs on the same chip, wafer-level testing can be executed on the fabricated devices. Our simulation results show that the triangular cross-section fishbone grating design can yield high collection efficiency ($\sim 31\%$) for studying the color center coupling with the integrated nanophotonic devices and initial fabrication results demonstrate the feasibility of producing the optimized designs with the RIBE process.

ACKNOWLEDGMENTS

We acknowledge support from NSF CAREER (Award 2047564) and AFOSR Young Investigator Program (Award FA9550-23-1-0266). Work at the Molecular Foundry was supported by the Office of Science, Office of Basic Energy Sciences, of the U.S. Department of Energy under Contract No. DE-AC02-05CH11231. Part of this study was carried out at the UC Davis Center for NanoMicro Manufacturing (CNM2). The authors would like to acknowledge the valuable support provided by Elnaz Hamdarsi and CNM2 staff member Vishal Narang.

AUTHOR DECLARATION

Conflict of Interest

The authors have no conflict of interest.

Author Contributions

PS modeled, analyzed and fabricated devices, SM developed the angle etching process, SD performed electron beam lithography, MR supervised the project.

DATA AVAILABILITY STATEMENT

The data that support the findings of this study are available upon reasonable request from the corresponding author Pranta Saha (prsaha@ucdavis.edu).

REFERENCES

[1]H. J. Kimble, Nature **453**, 1023 (2008).
[2]C. Monroe, Nature **416**, 238 (2002).
[3]K. Azuma, S. E. Economou, D. Elkouss, P. Hilaire, L. Jiang, H.-K. Lo, and I. Tzitrin, Reviews of Modern Physics **95**, 045006 (2023).
[4]V. A. Norman, S. Majety, Z. Wang, W. H. Casey, N. Curro, and M. Radulaski, InfoMat **3**, 869 (2021).
[5]B. Hensen, H. Bernien, A. E. Dréau, A. Reiserer, N. Kalb, M. S. Blok, J. Ruitenberg, R. F. Vermeulen, R. N. Schouten, C. Abellán, *et al.*, Nature **526**, 682 (2015).
[6]S. Majety, P. Saha, V. A. Norman, and M. Radulaski, Journal of Applied Physics **131** (2022).
[7]C. P. Anderson, E. O. Glen, C. Zeledon, A. Bourassa, Y. Jin, Y. Zhu, C. Vorwerk, A. L. Crook, H. Abe, J. Ul-Hassan, *et al.*, Science advances **8**, eabm5912 (2022).
[8]P. Cilibrizzi, M. J. Arshad, B. Tissot, N. T. Son, I. G. Ivanov, T. Astner, P. Koller, M. Ghezellou, J. Ul-Hassan, D. White, *et al.*, Nature Communications **14**, 8448 (2023).
[9]S. Castelletto, A. Peruzzo, C. Bonato, B. C. Johnson, M. Radulaski, H. Ou, F. Kaiser, and J. Wrachtrup, ACS Photonics **9**, 1434 (2022).
[10]D. M. Lukin, M. A. Guidry, and J. Vučković, PRX quantum **1**, 020102 (2020).
[11]P. Udvarhelyi, R. Nagy, F. Kaiser, S.-Y. Lee, J. Wrachtrup, and A. Gali, Physical Review Applied **11**, 044022 (2019).
[12]S. Majety, V. A. Norman, L. Li, M. Bell, P. Saha, and M. Radulaski, Journal of Physics: Photonics **3**, 034008 (2021).
[13]C. Babin, R. Stöhr, N. Morioka, T. Linkewitz, T. Steidl, R. Wörnle, D. Liu, E. Hesselmeier, V. Vorobyov, A. Denisenko, *et al.*, Nature materials **21**, 67 (2022).
[14]S. Majety, S. Strohauer, P. Saha, F. Wietschorke, J. J. Finley, K. Müller, and M. Radulaski, Materials for Quantum Technology **3**, 015004 (2023).
[15]P. Saha, S. Majety, and M. Radulaski, Scientific reports **13**, 4112 (2023).
[16]S. Majety, P. Saha, Z. Kekula, S. Dhuey, and M. Radulaski, MRS communications , 1 (2024).
[17]S. Majety, V. A. Norman, P. Saha, A. H. Rubin, S. Dhuey, and M. Radulaski, arXiv preprint arXiv:2405.07498 (2024).
[18]L. Cheng, S. Mao, Z. Li, Y. Han, and H. Fu, Micromachines **11**, 666 (2020).
[19]R. Marchetti, C. Lacava, L. Carroll, K. Gradkowski, and P. Minzioni, Photonics Research **7**, 201 (2019).
[20]V. A. Norman, S. Majety, A. H. Rubin, P. Saha, J. Simo, B. Palomarez, L. Li, P. B. Curro, S. Dhuey, S. Virasawmy, *et al.*, arXiv preprint arXiv:2401.10509 (2024).
[21]A. Faraon, I. Fushman, D. Englund, N. Stoltz, P. Petroff, and J. Vučković, Optics express **16**, 12154 (2008).
[22]X. Zhou, I. Kulkova, T. Lund-Hansen, S. L. Hansen, P. Lodahl, and L. Midolo, Applied Physics Letters **113** (2018).
[23]Y. Zhu, J. Wang, W. Xie, B. Tian, Y. Li, E. Brainis, Y. Jiao, and D. Van Thourhout, Optics express **25**, 33297 (2017).
[24]C. M. Caves and P. D. Drummond, Reviews of Modern Physics **66**, 481 (1994).
[25]P. C. Humphreys, B. J. Metcalf, J. B. Spring, M. Moore, X.-M. Jin, M. Barbieri, W. S. Kolthammer, and I. A. Walmsley, Physical review letters **111**, 150501 (2013).
[26]G. Son, S. Han, J. Park, K. Kwon, and K. Yu, Nanophotonics **7**, 1845 (2018).
[27]Y. Fu, T. Ye, W. Tang, and T. Chu, Photonics Research **2**, A41 (2014).
[28]M. J. Burek, C. Meuwly, R. E. Evans, M. K. Bhaskar, A. Sipahigil, S. Meesala, B. Machielse, D. D. Sukachev, C. T. Nguyen, J. L. Pacheco, *et al.*, Physical Review Applied **8**, 024026 (2017).
[29]J. Zhang, J. Yang, H. Lu, W. Wu, J. Huang, and S. Chang, Infrared Physics & Technology **71**, 542 (2015).
[30]J. Hadden, C. Maynard, D. M. Beggs, R. A. Taylor, and A. J. Bennett, Journal of Physics D: Applied Physics **55**, 474002 (2022).
[31]L. C. Andreani, D. Gerace, M. Passoni, A. Bozzola, and L. Carroll, in *2016 18th International Conference on Transparent Optical Networks (ICTON)* (IEEE, 2016) pp. 1–4.
[32]V. Vitali, T. Domínguez Bucio, C. Lacava, R. Marchetti, L. Mastronardi, T. Rutirawut, G. Churchill, J. Faneca, J. C. Gates, F. Gardes, *et al.*, Photonics Research **11**, 1275 (2023).
[33]Y. Ding, H. Ou, and C. Peucheret, Optics letters **38**, 2732 (2013).
[34]M. H. Lee, J. Y. Jo, D. W. Kim, Y. Kim, and K. H. Kim, Journal of the Optical Society of Korea **20**, 291 (2016).